Journal of Advanced Ceramics
2024, **13**(5): 666–678
https://doi.org/10.26599/JAC.2024.9220887

Research Article

Novel C_{sf}/SiBCN composites prepared by densifying C_{sf}/MA-SiBCN with the PIP process: Oxidation behavior and damage mechanism

Wenhao Dou[1,2], Daxin Li[1,2,✉], Bingzhu Wang[1,2], Zhihua Yang[1,2,3], Jun Chen[4], Dechang Jia[1,2,✉], Ralf Riedel[5], Yu Zhou[1,2,6]

[1] *Institute for Advanced Ceramics, School of Materials Science and Engineering, Harbin Institute of Technology, Harbin 150001, China*
[2] *Key Laboratory of Advanced Structural-Functional Integration Materials and Green Manufacturing Technology, Harbin Institute of Technology, Harbin 150001, China*
[3] *Chongqing Research Institute of HIT, Chongqing 401135, China*
[4] *Beijing Institute of Control Engineering, Beijing 100094, China*
[5] *Institut für Materialwissenschaft, Technische Universität Darmstadt, Darmstadt D-64287, Germany*
[6] *School of Materials Science and Engineering, Harbin Institute of Technology (Shenzhen), Shenzhen 518055, China*

Received: October 25, 2023; Revised: March 3, 2024; Accepted: March 30, 2024

Abstract: To improve the oxidation resistance of short carbon fiber (C_{sf})-reinforced mechanically alloyed SiBCN (MA-SiBCN) (C_{sf}/MA-SiBCN) composites, dense amorphous C_{sf}/SiBCN composites containing both MA-SiBCN and polymer-derived ceramics SiBCN (PDCs-SiBCN) were prepared by repeated polymer infiltration and pyrolysis (PIP) of layered C_{sf}/MA-SiBCN composites at 1100 °C, and the oxidation behavior and damage mechanism of the as-prepared C_{sf}/SiBCN at 1300–1600 °C were compared and discussed with those of C_{sf}/MA-SiBCN. The C_{sf}/MA-SiBCN composites resist oxidation attack up to 1400 °C but fail at 1500 °C due to the collapse of the porous framework, while the PIP-densified C_{sf}/SiBCN composites are resistant to static air up to 1600 °C. During oxidation, oxygen diffuses through preexisting pores and the pores left by oxidation of carbon fibers and pyrolytic carbon (PyC) to the interior of the matrix. Owing to the oxidative coupling effect of the MA-SiBCN and PDCs-SiBCN matrices, a relatively continuous and dense oxide layer is formed on the sample surface, and the interfacial region between the oxide layer and the matrix of the as-prepared composite contains an amorphous glassy structure mainly consisting of Si and O and an incompletely oxidized but partially crystallized matrix, which is primarily responsible for improving the oxidation resistance.

Keywords: mechanically alloyed SiBCN (MA-SiBCN); polymer-derived ceramics SiBCN (PDCs-SiBCN); short carbon fiber-reinforced SiBCN (C_{sf}/SiBCN) composites; polymer infiltration and pyrolysis (PIP); oxidation damage mechanism

1 Introduction

The aerospace industry is continually searching for lighter, high-strength thermostructural materials that perform under increasingly extreme conditions [1–5]. Interest in mechanically alloyed SiBCN (MA-SiBCN) ceramics is driven by their potential applications in high-temperature oxygen-sensitive environments [6]. Many MA-SiBCN materials can now offer a tantalizing combination of properties, including low density [7], good environmental resistance [8–10], and desirable strength [11,12]. Unfortunately, monolithic versions of MA-SiBCN suffer from one serious and obvious shortcoming, namely, low toughness. An effective way to overcome the low fracture toughness is to fabricate these materials as composites. One route is to prepare fiber-reinforced ceramic matrix composites. Coincidentally, ceramic/metal particle-reinforced [13], whisker-, and short fiber-reinforced [14,15] MA-SiBCN ceramic matrix composites have apparent toughness and reliability comparable to those of monoliths, although toughness increases at the expense of some loss in other characteristics.

However, in the existing molding methods, short carbon fiber (C_{sf}) reinforced MA-SiBCN (C_{sf}/MA-SiBCN) composites are generally densified at much higher temperatures (> 1800 °C), leading to the strength degradation of the fibers and strong interfacial bonding between the fibers and the matrix [14,15], which is detrimental to the strengthening and toughening effect of the fibers. For this reason, we developed a combination of low-temperature pressureless sintering (1100 °C) and layered C_{sf} preforms to produce amorphous C_{sf}/MA-SiBCN composites with pseudoplastic fracture characteristics [16]. In this case, crystallization of the MA-SiBCN matrix and degradation of the short fibers can be avoided, and a weak but not too weak interface can be achieved. However, a further issue in the design and processing of optimal amorphous C_{sf}/MA-SiBCN composites is their low density and subsequent unsatisfactory strength, which leads to poor oxidation resistance.

Polymer-derived ceramics SiBCN (PDCs-SiBCN) can be tailored effectively by controlling the initial reagent structures, chemical reactions, and processing parameters [17,18] to obtain

✉ Corresponding authors.
E-mail: D. Li, lidaxin@hit.edu.cn;
D. Jia, dcjia@hit.edu.cn

higher thermal stability [19–21] and good oxidation resistance [22,23], although it is difficult to fabricate dense monoliths and structural components. Nevertheless, the polymer-derived ceramic route combined with vacuum-assisted polymer infiltration [24–27] or pressure-assisted or low-temperature sintering [28–31] can offer better processing than simple precursor processing to obtain dense SiBCN composites. Therefore, novel dense C_{sf}/SiBCN composites prepared by densifying C_{sf}/MA-SiBCN via the polymer infiltration and pyrolysis (PIP) process immediately come to mind.

Research on the oxidation of MA-SiBCN and PDCs-SiBCN has focused mainly on the oxide scale structure and scale-forming mechanism. For example, Butchereit *et al.* [22] investigated the oxidation resistance of three PDCs-SiBCNs at 1300 and 1500 °C and found that an amorphous SiO_2 oxide layer transferred to crystallites in regions near bubbles, while other oxide zones were amorphous. Cinibulk and Parthasarathy [23] further reported a unique trilayer oxide structure of oxidized SiBCN fibers at 1500 °C: The outermost layer composed of cristobalite, the interlayer composed of amorphous silica, and the innermost layer composed of amorphous SiBCNO and turbostratic BN. In contrast, the dense amorphous MA-SiBCN ceramics oxidized at 1700 °C exhibited an external N-containing amorphous SiO_2 layer, an intermediate loose layer, and an internally unoxidized but crystallized MA-SiBCN matrix [9].

The introduction of carbon fibers (C_{sf} or continuous carbon fibers (C_{cf})) generally deteriorates the oxidation resistance of the SiBCN matrix, although a homogeneous and uniform distribution of carbon fibers is achieved. In this regard, Jia *et al.* [32] studied the oxidation behavior of C_{cf}/PDCs-SiBCN in static air, and the results clearly suggested different oxidation mechanisms at different oxidation temperatures: Carbon fibers were preferentially oxidized at low temperatures (1200–1500 °C), and subsequently, oxygen diffused into the PDCs-SiBCN matrix through the channels left from fiber oxidation. At higher temperatures (1600–1700 °C), nanosized SiC, Si_3N_4, and hexagonal boron nitride (h-BN) precipitates and a partially amorphous PDCs-SiBCN matrix were oxidized to form a dense passivating SiO_2 layer. In another contribution, Luan *et al.* [33] studied the oxidation behavior of C_{cf}/SiC-SiBCN under wet-oxygen environments and found that oxidation products of B_2O_3 and SiO_2 appeared on the sample surfaces, effectively hindering the internal diffusion of oxygen, but the oxidation damage mechanisms still need to be determined. For hot-pressed C_{sf}/MA-SiBCN [15], significant weight gain was measured for composites densified at lower sintering temperatures since substantial preexisting micropores and/or microcracks are the natural acceleration channels for oxygen diffusion.

Generally, the C_{cf}/PDCs-SiBCN and C_{sf}/MA-SiBCN composites exhibit different oxidation behaviors, which are argued to be the composition and microstructural differences between PDCs-SiBCN and MA-SiBCN. Although there is still disagreement about the oxidation behavior and scale growth mechanism of PDCs-SiBCN and MA-SiBCN, it is well accepted that a dense, passivating oxide scale consisting primarily of SiO_2 serves as a protective layer at high temperatures, thereby effectively inhibiting further oxidation and providing good oxidation resistance. To date, studies on the synergistic oxidative mechanisms between MA-SiBCN and PDCs-SiBCN are still in their infancy, and the oxidation behavior of multicomponent C_f/SiBCN composites (the matrix contains PDCs-SiBCN and MA-SiBCN) after oxidation at different temperatures needs to be further studied.

In this study, the amorphous porous C_{sf}/MA-SiBCN composite was densified by a repeated PIP process at 1100 °C using a polyborosilazane (PBSZ) precursor to finally obtain dense C_{sf}/SiBCN composites containing both MA-SiBCN and PDCs-SiBCN matrices. The effects of the PIP process on the oxidation behavior and damage mechanism of the C_{sf}/SiBCN composites at 1300–1600 °C were compared and discussed. In particular, the microstructure of the interfacial region between the oxide layer and the matrix of the composite was also revealed.

2 Materials and methods

2.1 Fabrication of C_{sf}/SiBCN composites

Porous C_{sf}/MA-SiBCN composites were prepared according to the method described in our previous paper [16]. In brief, short carbon fibers (T700SC 12K, Toray, Japan) with an average length of ~7 mm were ultrasonically dispersed in ethanol and filtered through a stainless-steel filter with a diameter of 30 mm. After natural drying, a thin short fiber cloth with an average mass of 0.0080 g (0.0075–0.0085 g) was prepared. MA-SiBCN powders were prepared by mechanically alloying graphite (C, 99.95% purity, 8000 mesh; Shanghai Macklin Biochemical Co., Ltd., China), hexagonal boron nitride (h-BN, 99.0% in purity, 0.6 μm, Advanced Technology and Materials Co., Ltd., China), and cubic silicon (c-Si, 99.99% purity, 9 μm; New Metal Materials Technology Co., Ltd., China) with a molar ratio of 3 : 1 : 2, and the mass fractions of Si, B, C, N, and O in the MA-SiBCN powders were measured by an inductively coupled plasma spectrometer (ICP; 5110 (OES), Agilent, USA), a carbon sulfur analyzer (HIR944, Wuxi High-speed Analyzer, China), and an oxygen nitrogen hydrogen analyzer (EMGA-830, Horiba, Japan), and were 41.87, 9.12, 30.25, 6.79, and 4.14 wt%, respectively.

The content of the C_{sf}/MA-SiBCN composites refers to that of "C_{sf}/SiBCN-4" from our previous paper [16]. Phenolic resin (P195710, Shanghai Aladdin Biochemical Technology Co., Ltd., China) was mixed with ethanol (mass ratio of 1.01). MA-SiBCN powders were mixed with ethanol (mass ratio of 2.72) at the same time. Then, the ethanolic solution of the phenolic resin and the ethanolic suspension containing MA-SiBCN powders were mixed together, followed by stirring and ultrasonic vibration to obtain the MA-SiBCN slurry. The as-fabricated short fiber cloths were placed in a mold and infiltrated with ~0.25 g of the MA-SiBCN slurry. After this process was repeated for 40 layers, the mold was heated at 50 °C for 12 h to evaporate the ethanol, and then the phenolic resin was cured at 100 °C for 30 min and 150 °C for 1 h. During the curing process, 300 g in weight (~3.44 kPa) was placed above the mold to prevent foaming and delamination. Finally, the demolded compact was placed in a tube furnace (RHTH 120-600/18, Nabertherm GmbH, Germany) at a heating rate of 2 °C/min to 1100 °C for 4 h and then cooled to 600 °C at 3 °C/min under a high-purity nitrogen atmosphere to obtain porous C_{sf}/MA-SiBCN composites (density: 1.24 g/cm^3 and open porosity: 45.71%, as shown in Table 1).

Dense C_{sf}/SiBCN composites were obtained from porous C_{sf}/MA-SiBCN by the PIP process. First, polyborosilazane (KH-SiBCN-C, Institute of Chemistry, Chinese Academy of Sciences, China), which is a precursor of PDCs-SiBCN with a viscosity lower than 100 CP and a molecular weight (M_n) of 600–900, was stirred with 1 wt% dicumyl peroxide (DCP; D100481, Shanghai Aladdin Biochemical Technology Co., Ltd., China) to prepare a PBSZ–DCP solution. Porous C_{sf}/MA SiBCN was placed in a container and infiltrated with PBSZ–DCP solution under vacuum for 45 min. Then, the infiltrated sample was crosslinked at 170 °C for 2 h (ramping rate of 1 °C/min) and pyrolyzed at 1100 °C for 2 h (ramping rate of 5 °C/min) in a tube furnace under a

Table 1 Density and porosity of C_{sf}/MA-SiBCN and the as-prepared C_{sf}/SiBCN composites after different numbers of PIP cycles

Sample	Density (g/cm³)	Open porosity (%)	Mass gain after each PIP cycle (%)
PIP-0	1.24	45.7	—
PIP-1	1.37	31.1	10.1
PIP-2	1.49	23.9	5.3
PIP-3	1.58	15.2	3.9
PIP-4	1.65	11.4	2.2
PIP-5	1.69	9.8	0.8

high-purity nitrogen atmosphere to obtain the composites. The mass fractions of Si, B, C, N, and O of PDCs-SiBCN measured by the same method as MA-SiBCN are 37.49, 8.78, 20.70, 17.97, and 1.32 wt%, respectively, after pyrolysis at 1100 °C under nitrogen. The polymer infiltration and pyrolysis process was repeated until the mass gain was less than 1%. The as-prepared composites are marked as PIP-*X* (*X* represents the number of PIP cycles), and the C_{sf}/MA-SiBCN composite is marked as PIP-0.

2.2 Oxidation test

C_{sf}/MA-SiBCN and the as-prepared C_{sf}/SiBCN composites were processed into small pieces (3 mm × 4 mm × 5 mm) for the oxidation test. The samples were polished on each surface using a diamond grinding disc and ultrasonically cleaned with ethanol three times before oxidation. The oxidation test was performed in a tube furnace under static air at 1300, 1400, 1500, and 1600 °C with holding time of 5 h. The furnace was heated to the oxidation temperature at a rate of 5 °C/min and cooled to 900 °C at 5 °C/min.

2.3 Characterizations

The density and porosity of the PIP-*X* samples were measured using the Archimedes method. The mass change per surface area of the composites after oxidation was calculated to evaluate the oxidation performance. The phase compositions of the composites before and after oxidation were measured on a 4 mm × 5 mm surface by an X-ray diffractometer (XRD; Empyrean, PANalytical B.V., the Netherlands) with a scanning speed of 10 (°)/min. The formed oxide layer was characterized by a tip-enhanced laser confocal Raman spectrometer (inVia-Reflex, Renishaw, UK) using a 532 nm excitation source. An X-ray photoelectron spectrometer (XPS; ESCALAB 250XI, Thermo Scientific, USA) was used to characterize the chemical valence state of the constituting elements of the oxide layer. Thermal analysis of the PIP-*X* samples was performed using a simultaneous thermal analyzer (STA449F3, NETZSCH, Germany) in flowing air from room temperature to 1550 °C with a heating rate of 10 °C/min. The microstructure of the composites after oxidation was observed by an scanning electron microscope (SEM; SU5000, Hitachi, Japan). The microstructure between the oxide layer and the matrix of the composite was characterized via sample preparation using a focused ion beam (FIB) in a double-focused ion beam scanning electron microscope (TESCAN AMBER, TESCAN, Czech Republic), which was observed by a transmission electron microscope (TEM; Talos F200x G2, FEI, USA).

3 Results and discussion

3.1 Oxidation behavior of composites at different temperatures

As shown in Table 1, the mass gain of each PIP cycle decreases gradually and is less than 1% after the 5th PIP cycle, so 5 cycles are used as the number of PIP cycles. The density of the as-prepared C_{sf}/SiBCN composites gradually increased to 1.69 g/cm³, the porosity decreased to 9.8% after the 5th PIP, the cross-sectional morphology became dense, and the pore size gradually decreased (Fig. S1 in the Electronic Supplementary Material (ESM)) with increasing the number of PIP cycles, demonstrating that the PIP process successfully achieved low-temperature densification of the C_{sf}/MA-SiBCN composites. Optical images of the C_{sf}/MA-SiBCN and the as-prepared C_{sf}/SiBCN composites after oxidation are displayed in Fig. 1. It is obvious that the samples oxidized at 1300 and 1400 °C show slight oxidation and retain their macroscopic appearance. The mass changes per surface area of the PIP-0 and PIP-5 samples after oxidation at 1300 and 1400 °C are similar (Table 2), suggesting similar degrees of oxidation at low temperatures. When the oxidation temperature increases to 1500 °C, sample PIP-0 reveals severe surface damage, while samples PIP-1–5 maintain their macrostructural integrity, and the surface is obviously covered with an oxide layer. In addition, the mass change per surface area of sample PIP-5 is lower than that of sample PIP-0 after oxidation at 1500 °C (Table 2) because of the lower porosity (Table 1) and the formation of a continuous oxide layer (Fig. 1(c)), which also explains the change in the macroscopic appearance of the composites (Fig. 1(c)). At 1600 °C, the main structure of sample PIP-0 collapses because of intense oxidation caused by the high porosity (Table 1), and the macroscopic morphology gradually tends to be complete with the increase in the number of PIP cycles due to the lower porosity and the protective oxide layer. Therefore, the mass loss of sample PIP-0 is greater than that of sample PIP-5 (Table 2), indicating that the oxidation resistance of the composites improves after the PIP process.

3.2 Effect of oxidation temperature on surface composition

Figure S2 in the ESM shows the XRD patterns of the composites before oxidation. The composites remained amorphous after repeated PIP processing at 1100 °C. Figure 2 shows the XRD patterns of the composites after oxidation at different temperatures. After oxidation at 1300 and 1400 °C, the surface composition of sample PIP-0 is mainly composed of an amorphous glassy phase. The reason is as follows. The oxidation products of the amorphous MA-SiBCN powders after oxidation are an amorphous glassy phase mainly containing Si and O according to Ref. [34], so the phase composition on the surface of sample PIP-0 after oxidation mainly contains an amorphous glassy phase at 1300 °C. However, a small amount of B_2O_3 may volatilize, which causes the crystallization of SiO_2 at 1400 °C [35], so cristobalite (PDF#39-1425) is detected on the surface of sample PIP-0 at 1400 °C. In contrast, the main phase on the surface of the as-prepared composites is cristobalite (PDF#39-1425) at 1300 and 1400 °C because the surface of the oxidized PDCs-SiBCN mainly

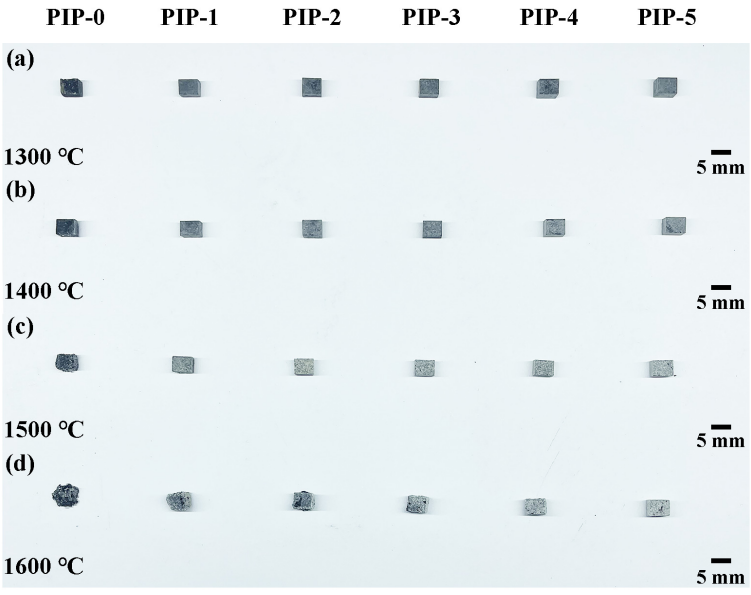

Fig. 1 Optical images of C_{sf}/MA-SiBCN and the as-prepared C_{sf}/SiBCN composites after oxidation at (a) 1300 °C, (b) 1400 °C, (c) 1500 °C, and (d) 1600 °C for 5 h.

Table 2 Mass change per surface area of the PIP-0 and PIP-5 samples after oxidation at different temperatures for 5 h

Oxidation temperature (°C)	Mass change per surface area (mg/mm²)	
	PIP-0	PIP-5
1300	−0.10	−0.14
1400	−0.11	−0.10
1500	−0.23	−0.15
1600	−0.34	−0.14

consists of cristobalite (Fig. S3 in the ESM). The different oxidation products between MA-SiBCN and PDCs-SiBCN may be attributed to the different contents of B. The B content of MA-SiBCN is higher than that of PDCs-SiBCN, as mentioned above, so it can be inferred that MA-SiBCN tends to generate more B_2O_3 during oxidation, which easily forms amorphous glass with SiO_2. In contrast, the B content of PDCs-SiBCN is lower than that of MA-SiBCN, which forms a small amount of B_2O_3 during oxidation, so most of the SiO_2 tends to transform into the cristobalite phase after oxidation of PDCs-SiBCN [35]. When the oxidation temperature increased to 1500 °C, the amorphous glassy phase covered the surface of sample PIP-0, and the cristobalite diffraction intensity at 1500 °C increased for the as-prepared composites compared to that at 1400 °C. At 1600 °C, severe oxidation occurs for sample PIP-0 (Fig. 1), forming a large amount of amorphous glass. The diffraction peak intensity of cristobalite somewhat decreases in the PIP-processed composites compared to that after oxidation at 1500 °C. The possible reason may be that high temperatures largely promote the formation of amorphous glass between a large amount of B_2O_3 and SiO_2

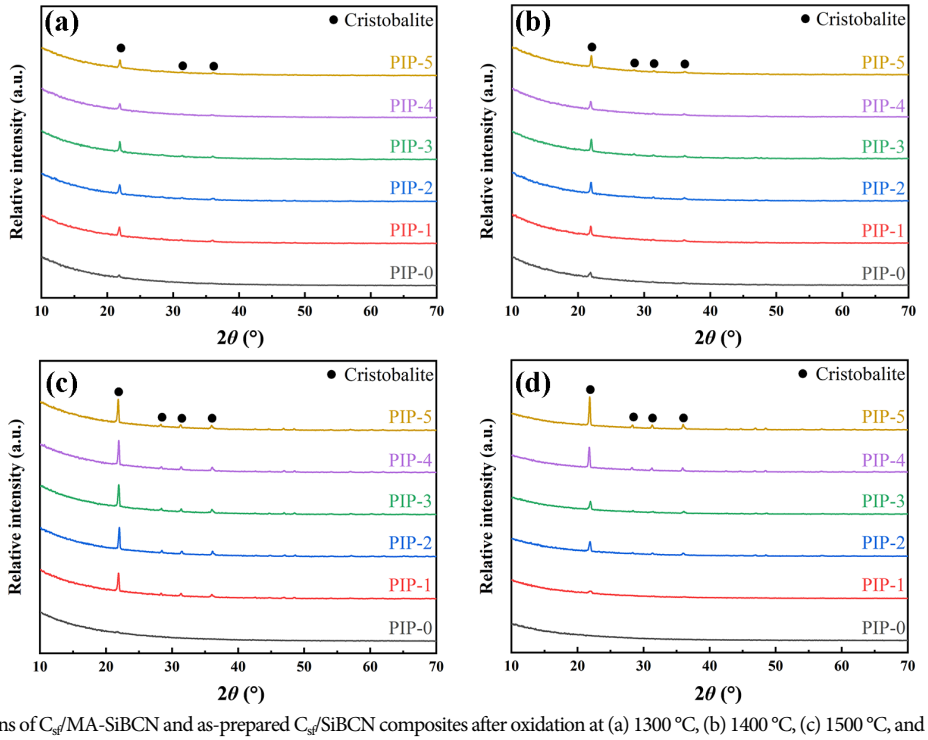

Fig. 2 XRD patterns of C_{sf}/MA-SiBCN and as-prepared C_{sf}/SiBCN composites after oxidation at (a) 1300 °C, (b) 1400 °C, (c) 1500 °C, and (d) 1600 °C for 5 h.

according to Ref. [10], which is greater than the volatilization of B_2O_3, which results in the crystallization of SiO_2 [35]. In addition, as the number of PIP cycles increases, the diffraction peak intensity of cristobalite increases at 1500 and 1600 °C. In summary, after oxidation, the surface of sample PIP-0 is mainly composed of amorphous glass. However, when PDCs-SiBCN were introduced, as the oxidation temperature increased, cristobalite was detected on the surface due to the different oxidation behaviors of MA-SiBCN and PDCs-SiBCN.

Figure 3 shows the Raman spectra of the PIP-*X* samples after oxidation at different temperatures for 5 h. At oxidation temperatures of 1300 and 1400 °C, the G and D peaks of graphite and the vibration peaks of cristobalite (~114, ~231, and ~440 cm^{-1}) are detected (Figs. 3(a) and 3(b)) for the as-prepared composites, which is consistent with the XRD results. On the surface of PDCs-SiBCN, only the G and D bands of carbon can be detected and tend to merge into a broad peak (Fig. S4 in the ESM), suggesting a low degree of oxidation for PDCs-SiBCN at these temperatures. When the oxidation temperature is greater than 1400 °C, the G and D bands almost disappear (Figs. 3(c) and 3(d)), indicating that the surface of the samples is free of carbon after oxidation at those high temperatures. Moreover, the vibration band of cristobalite can be detected on the PDCs-SiBCN surface (Fig. S4 in the ESM). At 1500 and 1600 °C, sample PIP-0 exhibited a wide band between 50 and 500 cm^{-1}, indicating the presence of amorphous silica [36], while cristobalite was detected in all the other PIP samples (Figs. 3(c) and 3(d)). Therefore, as the oxidation temperature increases, the G and D bands disappear, and amorphous silica and cristobalite are the main phases of the oxide layer of samples PIP-0 and PIP-1–5, respectively.

As shown in Fig. S5 in the ESM, before oxidation, sample PIP-5 includes Si–C, Si–O, and B–N bonds. In contrast, after oxidation at 1500 °C for 5 h (Fig. 4), silicon in the oxide layer is present in the form of Si–O bonds without Si–C bonds, while oxygen forms O–Si bonds, and boron and nitrogen are not detected. The reason is that BN(C), which is the crystallized product of the matrix, is prone to oxidation to produce B_2O_3(g), NO_x(g), and CO_x(g) [9]. The XPS survey spectrum displayed in Fig. 4(a) clearly indicates that the oxide layer is mainly composed of Si and O, which is consistent with the Raman results.

3.3 Effect of oxidation temperature on microstructure

The SEM images in Fig. 5 show the surface morphology of the PIP-*X* samples after oxidation at different temperatures for 5 h. At 1300 °C, some large pores exist on the surface of the PIP-0 sample, which is relatively smooth and flat and covered by a film-like substance (Fig. 5(a1)). Based on the XRD results, it is concluded that the film-like surface is composed of amorphous glass. As the number of PIP cycles increases, the surface morphology changes remarkably. Some particles appear on the surface, which is similar to the surface morphology of PDCs-SiBCN after oxidation (Fig. S6 in the ESM), and the areas under the particles are dense (Figs. 5(a2) and 5(a3)), further indicating the formation of a protective oxide layer after the PIP process. Compared with that at 1300 °C, the surface layer of the three composites at 1400 °C is somewhat dense. When the oxidation temperature reaches 1500 °C, the surface of sample PIP-0 contains large cracked bubbles because of intense oxidation (Fig. 1(c)). According to the XRD and Raman results, the surface is covered by amorphous glass. The surface morphology of samples PIP-3 and PIP-5 is completely different from that of sample PIP-0, and there are small particles on the surface (Figs. 5(c2) and 5(c3)). Based on the XRD results, the enriched Si and O detected by EDS (Fig. 6) and the surface morphology of PDCs-SiBCN after oxidation (Fig. S6(c1) in the ESM), these particles were determined to be cristobalite. When the oxidation temperature increases to 1600 °C, the surface of sample PIP-0 still shows a glassy appearance, including residual pores, but without bubbles left by volatilization of B_2O_3, which indirectly confirms that most of the B_2O_3 combines with SiO_2 to form amorphous glass, while structural integrity is maintained for samples PIP-3 and PIP-5. However, some bubbles formed on the surface of PDCs-SiBCN (Fig. S6(d1) in the ESM), which may have

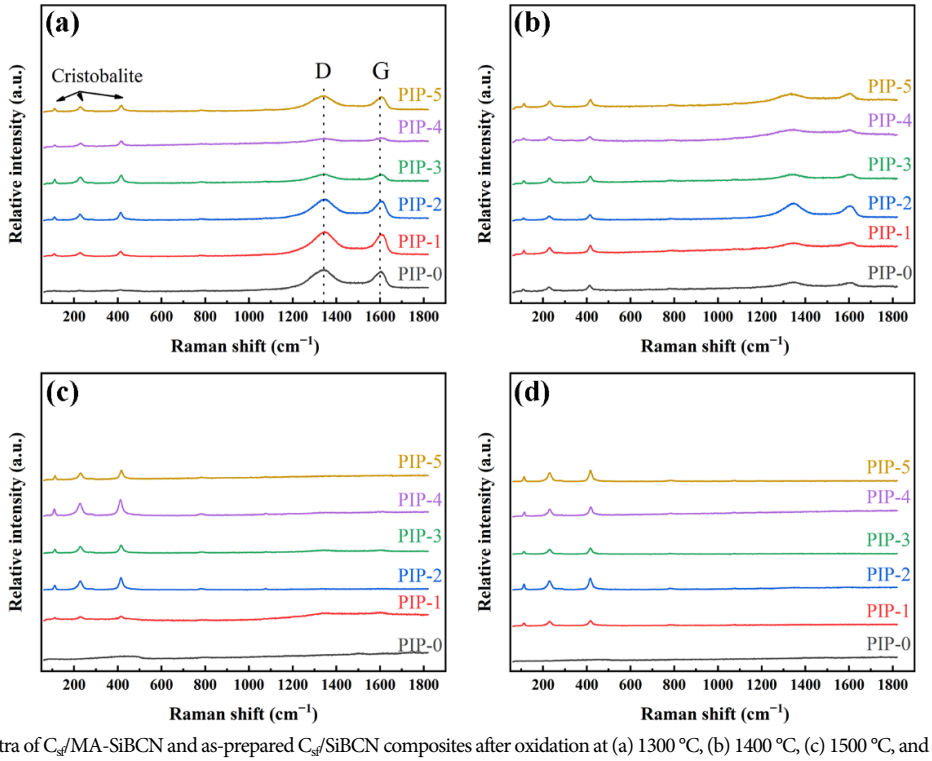

Fig. 3 Raman spectra of C_{sf}/MA-SiBCN and as-prepared C_{sf}/SiBCN composites after oxidation at (a) 1300 °C, (b) 1400 °C, (c) 1500 °C, and (d) 1600 °C for 5 h.

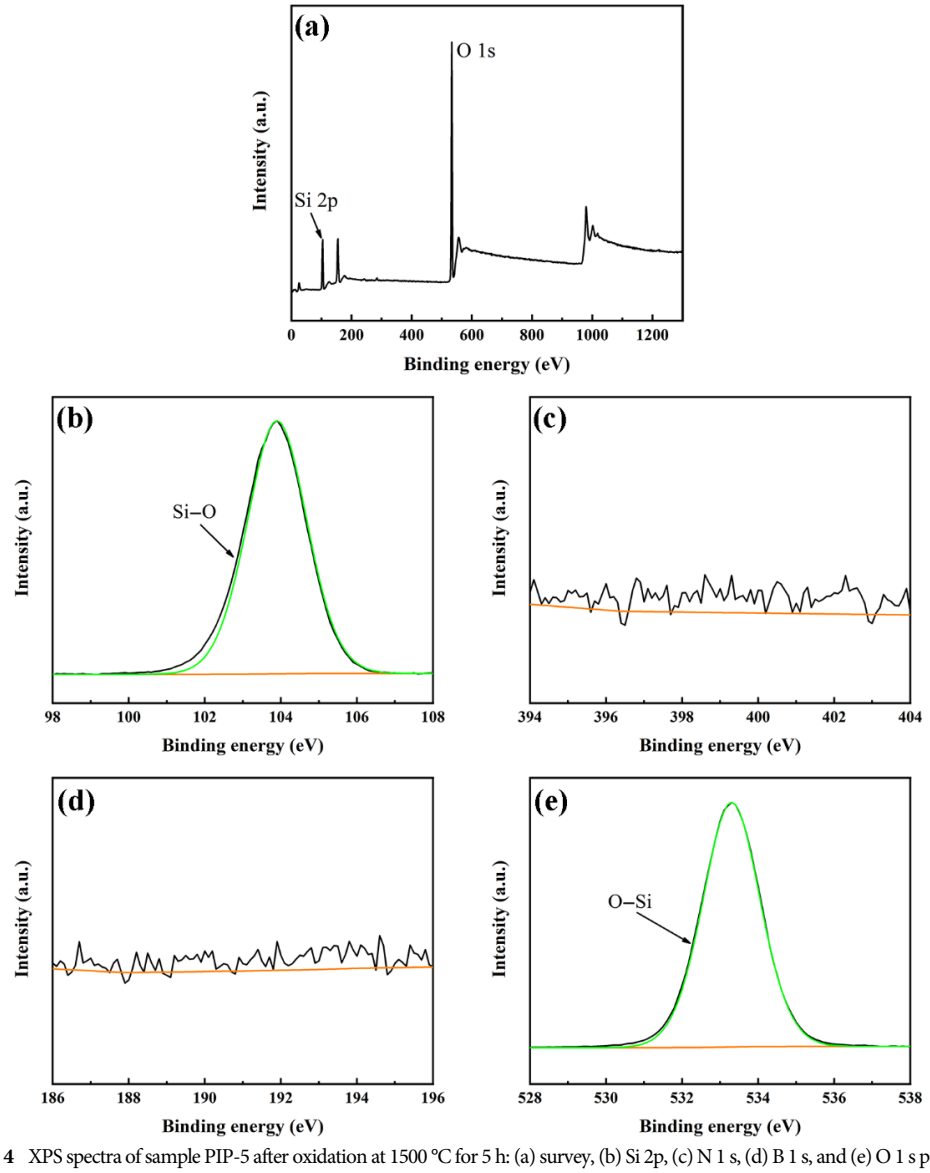

Fig. 4 XPS spectra of sample PIP-5 after oxidation at 1500 °C for 5 h: (a) survey, (b) Si 2p, (c) N 1 s, (d) B 1 s, and (e) O 1 s peaks.

been caused by the volatilization of B_2O_3, so it can be inferred that the volatilization of B_2O_3 causes the crystallization of SiO_2 to form the cristobalite phase [35], which is detected on the surface of PDCs-SiBCN (Fig. S3 in the ESM).

Figure 7 shows the cross-sectional morphologies of the PIP-*X* samples after oxidation at different temperatures for 5 h. After oxidation at 1300 and 1400 °C, there are many large pores in the cross-section of the PIP-0 sample, while few pores exist in the cross-sections of the PIP-3 and PIP-5 samples. These pores are formed by preferential oxidation of the carbon fibers [32,37] and pyrolytic carbon (PyC) derived from the phenolic resin in the matrix. At 1500 °C, an amorphous glassy phase appears on the cross-section and around the pores of sample PIP-0 (Fig. 7(c1)). The surfaces of the PIP-3 and PIP-5 composites contain a loose and porous oxide layer due to the presence of PDCs-SiBCN, and sample PIP-5 exhibits a low degree of internal oxidation (Fig. S7 and Table S1 in the ESM) due to the formation of a protective oxide layer (Figs. 7(c2) and 7(c3)). After oxidation at 1600 °C, significant oxidation inside sample PIP-0 is visible (Fig. 7(d1)) without the formation of a continuous oxide layer because of its high porosity. However, samples PIP-3 and PIP-5 also show a loose oxide layer on the surface but a dense region close to the composite, which adheres tightly to the composite and could hinder oxygen diffusion. The microstructure of this dense region is studied in TEM analysis.

Figure 8 shows the cross-section and elemental distribution of sample PIP-5 after oxidation at 1500 °C for 5 h. Si and O are mainly enriched in the oxide layer. During the oxidation process, carbon fibers and PyC are preferentially oxidized, leaving pores [32,37]. Oxygen is also enriched around the internal pores, indicating that oxygen diffuses to the interior through the pores.

In Fig. 9(a), the interfacial area between the oxide layer and the matrix of sample PIP-5 after oxidation at 1500 °C for 5 h is chosen for the FIB process. The selected area shows a dense structure with two distinct regions, the oxidized region and the incomplete oxidized matrix in the upper right corner (Fig. 9(b)). The detailed microstructure of the interfacial area is shown in Fig. 10. An incomplete oxidized matrix is embedded in the oxidized region without direct exposure to oxygen, which results in negligible crystallization and the formation of a small number of nanocrystals (Fig. 10(c)). However, further analysis by high-resolution TEM (HR-TEM) indicated that some turbulent BN(C)

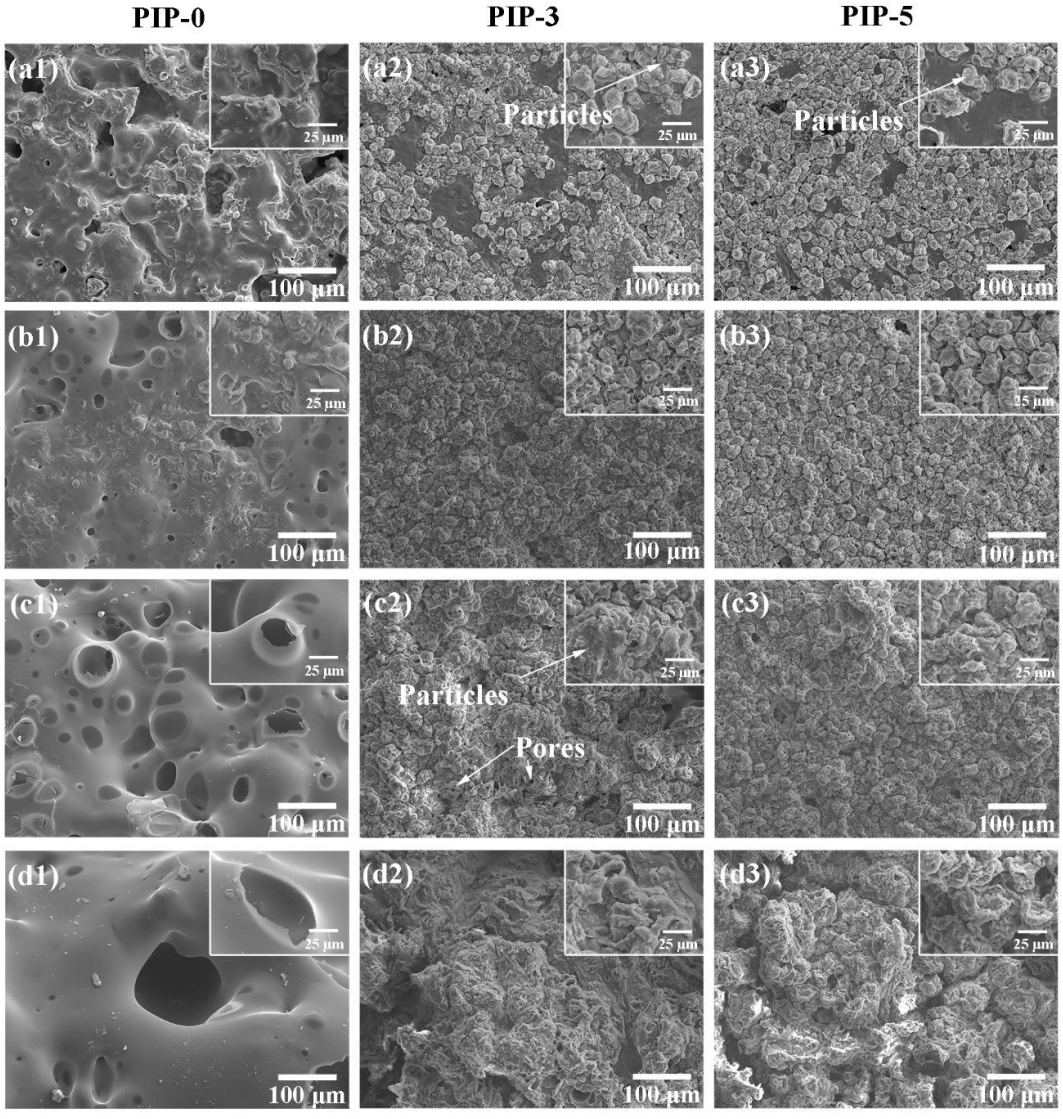

Fig. 5 Surface morphologies of C_{sf}/MA-SiBCN and as-prepared C_{sf}/SiBCN composites after oxidation at (a1–a3) 1300 °C, (b1–b3) 1400 °C, (c1–c3) 1500 °C, and (d1–d3) 1600 °C for 5 h.

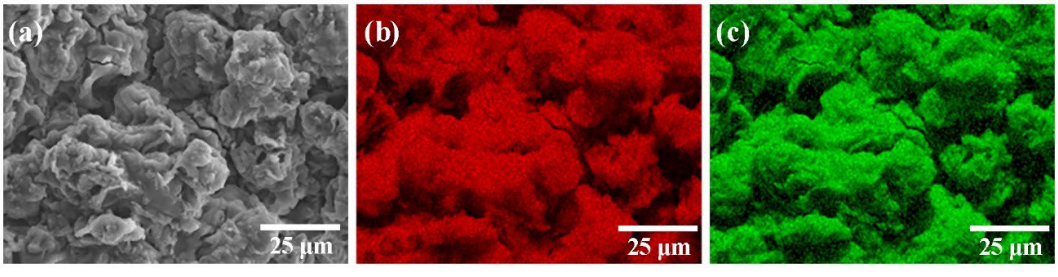

Fig. 6 (a) SEM image and EDS mappings for (b) Si and (c) O of surface of sample PIP-5 after oxidation at 1500 °C for 5 h.

grains precipitated close to the interface with an interplanar spacing of ~0.33 nm (Figs. 10(e) and 10(f)). The oxidized region near the composite also exhibits an amorphous structure according to the selected area electron diffraction (SAED) image in Fig. 10(d), and cristobalite detected by XRD is not observed, possibly because cristobalite is formed on the surface. The HR-TEM images displayed in Figs. 10(e) and 10(f) clearly show that the oxidized region near the composite is a dense structure with a clear boundary to the incomplete oxidized matrix, which plays an important role in the oxidation resistance.

Figure 11 shows the element mappings of the interface area of sample PIP-5 after oxidation at 1500 °C for 5 h. Si and O are mainly distributed in the oxidized region. Moreover, O is not significantly enriched in the incomplete oxidized matrix, indicating that the dense structure of the oxide layer near the matrix primarily hinders oxygen diffusion and protects the inner materials from oxidation attacks.

3.4 Oxidative damage mechanism

During the oxidation process, composites undergo not only

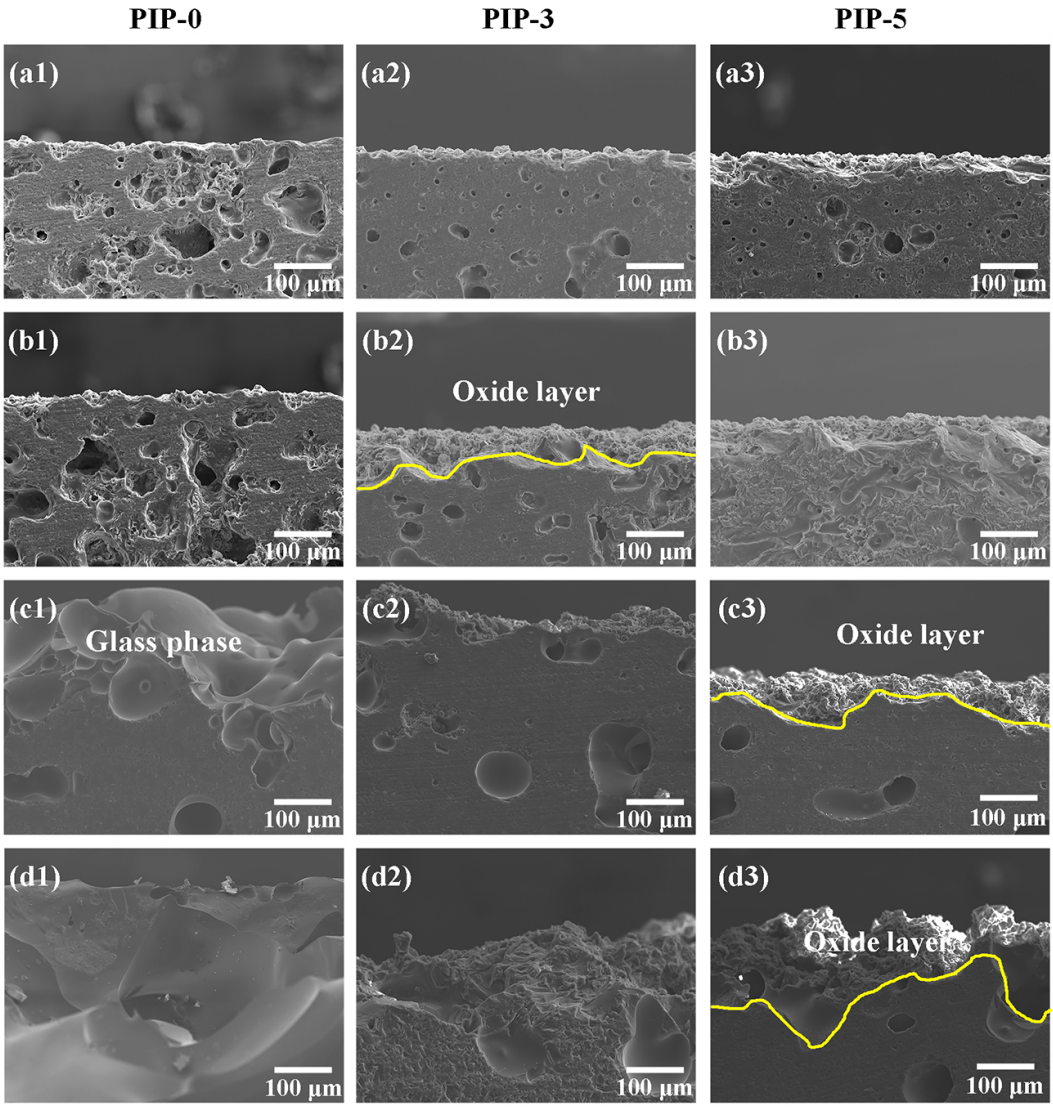

Fig. 7 Cross-sectional morphologies of C_{sf}/MA-SiBCN and as-prepared C_{sf}/SiBCN composites after oxidation at (a1–a3) 1300 °C, (b1–b3) 1400 °C, (c1–c3) 1500 °C, and (d1–d3) 1600 °C for 5 h.

oxidation but also crystallization of the matrix in the composites. To illustrate the effect of crystallization on the oxidation behavior, the phase compositions of the matrix and composites after high-temperature treatment under N_2 at a temperature consistent with the oxidation temperature are shown in Figs. S8 and S9 in the ESM. The main crystallization products of MA-SiBCN are SiC and BN(C), while those of PDCs-SiBCN are SiC with a lower degree of crystallization (Fig. S8(b) in the ESM). The possible reactions that may occur during oxidation are as Reactions (1)–(6) [9,10,32]:

$$2C(s) + O_2(g) \rightarrow 2CO(g) \quad (1)$$

$$C(s) + O_2(g) \rightarrow CO_2(g) \quad (2)$$

$$4/3BN(s) + O_2(g) \rightarrow 2/3B_2O_3(l) + 2/3N_2(g) \quad (3)$$

$$B_2O_3(l) \rightarrow B_2O_3(g) \quad (4)$$

$$2/3SiC(s) + O_2(g) \rightarrow 2/3SiO_2(l) + 2/3CO(g) \quad (5)$$

$$SiC(s) + O_2(g) \rightarrow SiO(g) + CO(g) \quad (6)$$

Figure 12 shows that within the oxidation temperature range, the standard Gibbs free energy of each reaction is negative, indicating that all the reactions can occur thermodynamically. During oxidation, carbon fibers and PyC derived from phenolic resin in the composites are oxidized (Reactions (1) and (2)) from 600 to 800 °C, during which significant weight loss and exothermic peaks appear (Fig. 13) because the activation energy of the reaction is low (15 kJ/mol, > 700 °C) [37]. At 1300 and 1400 °C, SiC nanocrystals form (Fig. S8(a) in the ESM), and oxidation of the SiC nanocrystals occurs along the pore channels left by the oxidation of carbon fibers (Fig. 7) and preexisting pores (Fig. S1 in the ESM) via Reactions (5) and (6) almost without the formation of an oxide layer on the surface but around the pore channels (Figs. 7(a) and 7(b)). Thus, no obvious mass change is found (Fig. 13 and Table 2). As the oxidation temperature increases, oxygen continues to diffuse toward the matrix around the pores. Due to the high porosity of sample PIP-0 (Table 1), oxidation occurs

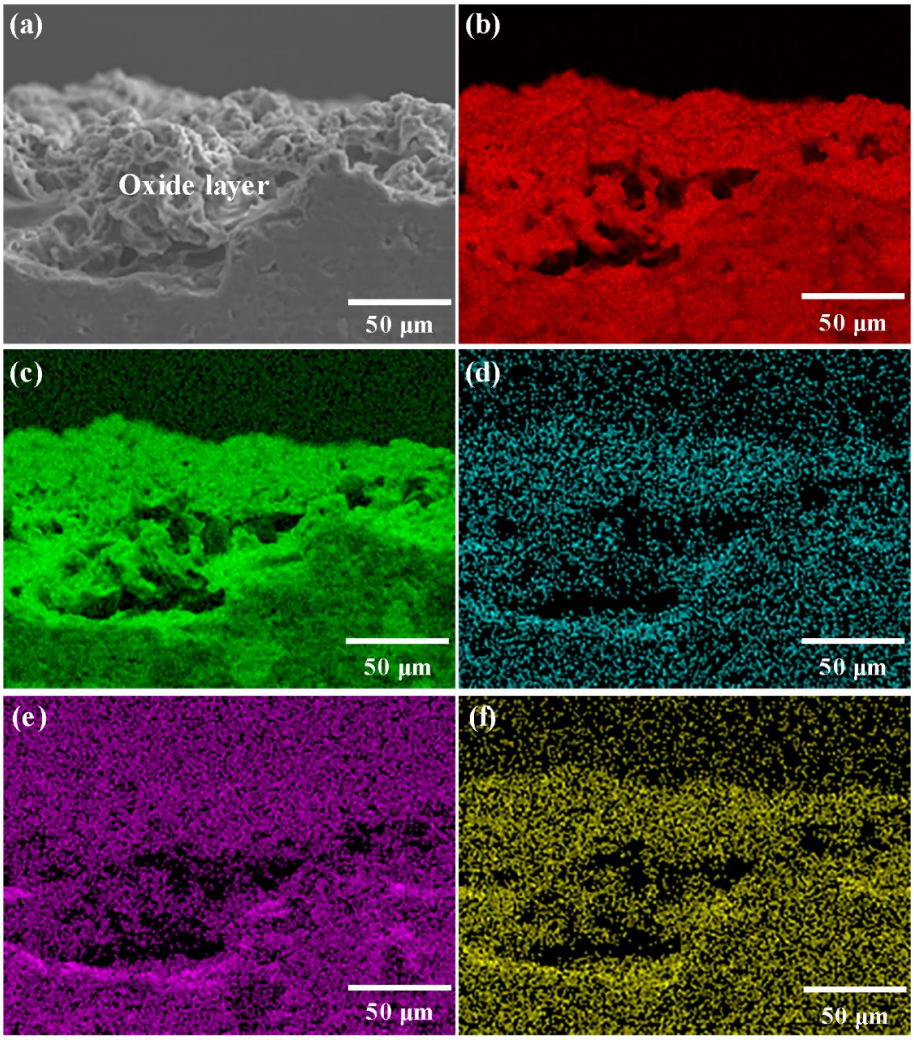

Fig. 8 (a) SEM image and EDS mappings for (b) Si, (c) O, (d) B, (e) C, and (f) N of cross-sections of sample PIP-5 after oxidation at 1500 °C for 5 h.

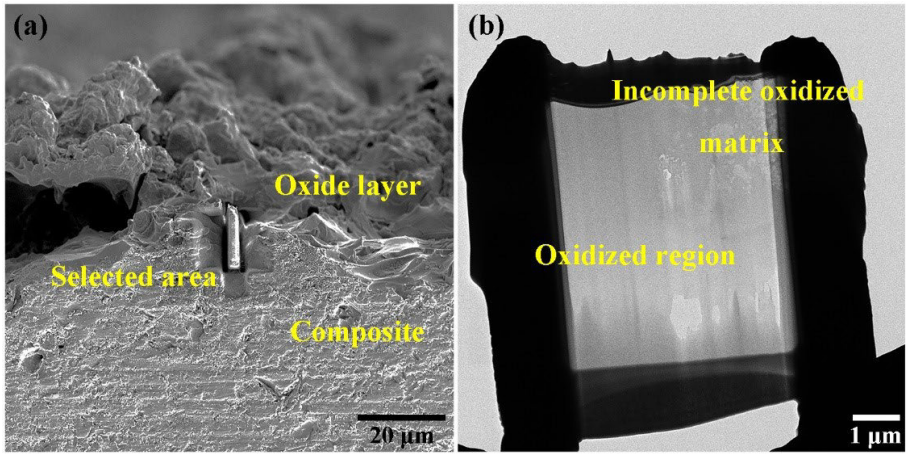

Fig. 9 Microstructure at interface between oxide layer and matrix of sample PIP-5 after oxidation at 1500 °C for 5 h: (a) selected area for FIB process and (b) processed specimen for TEM observation.

rapidly, and the surface does not form a continuous oxide layer, resulting in an obvious mass change (Fig. 13(a) and Table 2) and the collapse of the macrostructure. After the PIP process, the reduced porosity slows the degree of oxidation to some extent, so the SiBCN matrix is passively oxidized to form an oxide layer through Reactions (3) and (5) on the surface and around the pores (Figs. 7(c2) and 7(c3)). The formation of an oxide layer with a dense structure close to that of the composite combined with the outermost cristobalite particles is attributed to the difference in oxidation between MA-SiBCN and PDCs-SiBCN, which hinders oxygen diffusion with a negligible mass change (Fig. 13(b)) and improves the oxidation resistance compared to that of sample

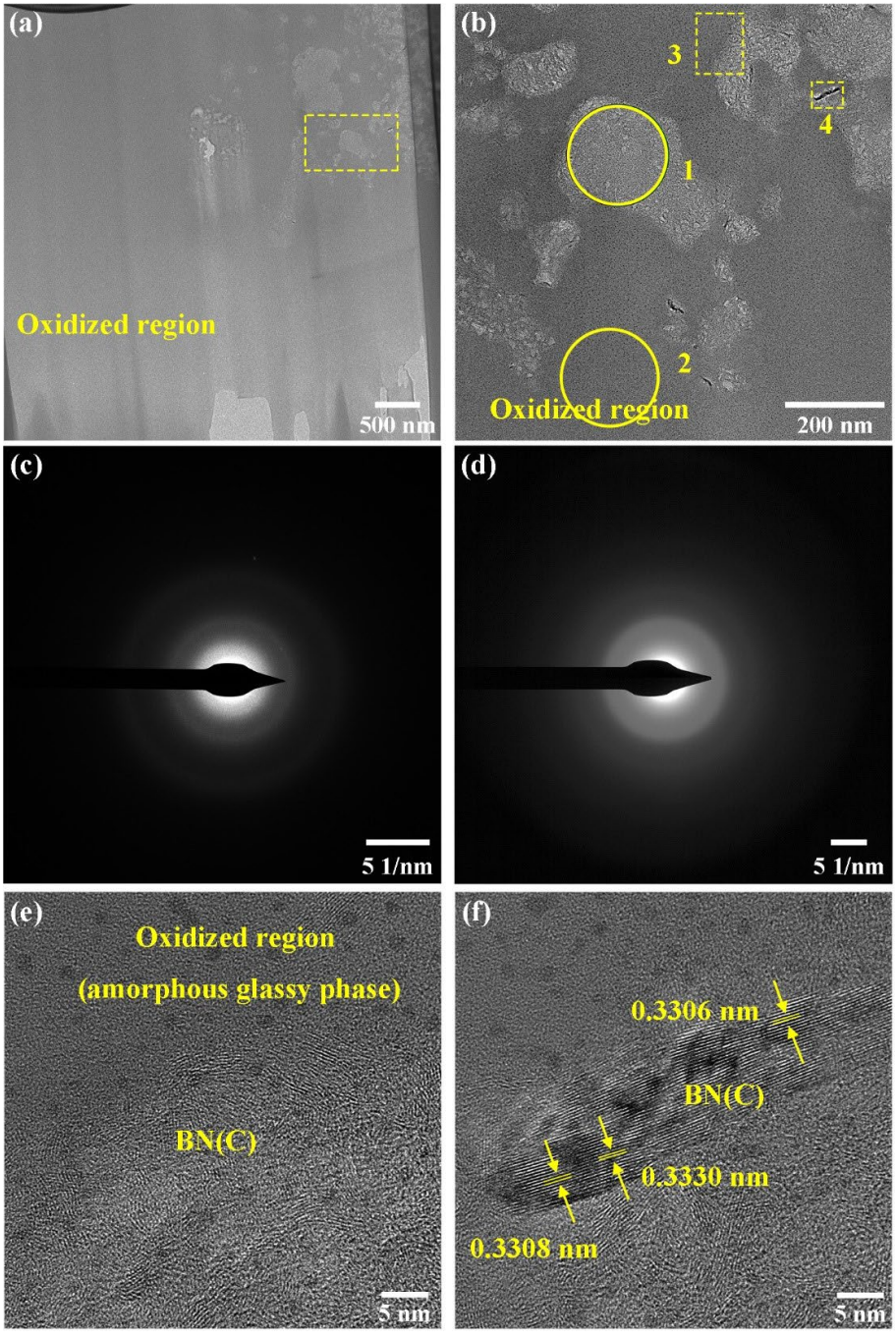

Fig. 10 TEM images of interface between oxide layer and matrix of sample PIP-5 after oxidation at 1500 °C for 5 h: (a) bright field image; (b) high-magnification image of yellow region in (a); (c, d) SAED images of regions 1 and 2 in (b); (e, f) HR-TEM images of regions 3 and 4 in (b).

PIP-0. However, oxidative mass gain cannot compensate for the significant mass loss caused by carbon fibers and PyC (Fig. 13), so overall, the composites exhibit mass loss after oxidation (Table 2).

4 Conclusions

The novel C_{sf}/SiBCN composites were prepared using a simple layering process combined with the PIP process using polyborosilazane as the PDCs-SiBCN precursor. The oxidation behavior of the composites at different temperatures was studied. The main conclusions are as follows:

1) The oxidation resistance of the composites significantly improved after the PIP process. The C_{sf}/MA-SiBCN framework collapsed at 1500 °C, while the composites containing PDCs-SiBCN prepared via PIP cycling still maintained macroscopic structural integrity up to 1600 °C.

2) With increasing the oxidation temperature from 1300 to 1600 °C, the oxidized surface of the C_{sf}/MA-SiBCN composite forms some bubbles and pores, which are mainly composed of amorphous glass mainly containing Si and O, while that of the C_{sf}/SiBCN composites prepared by the PIP process forms a continuous oxide layer covering the surface, and cristobalite is detected on the surface due to the coupling oxidation behavior of MA-SiBCN and PDCs-SiBCN.

3) During oxidation at 1300–1600 °C, carbon fibers and PyC

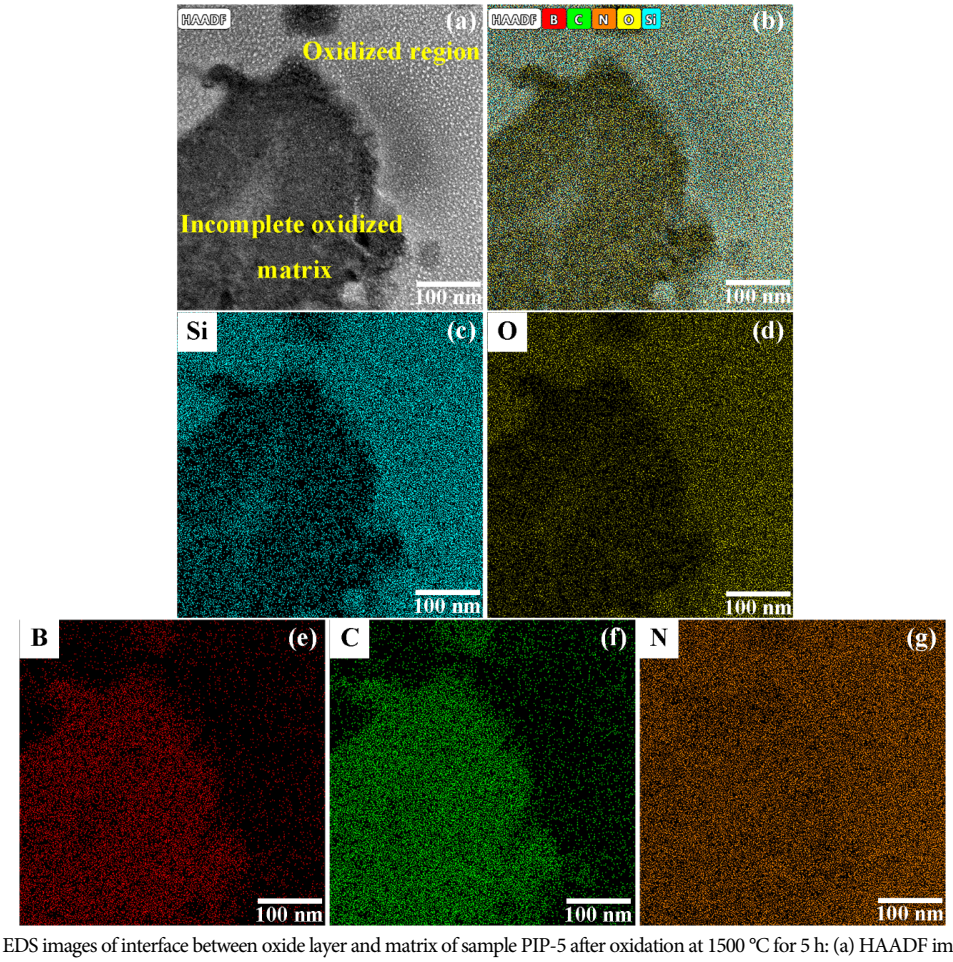

Fig. 11 HAADF and EDS images of interface between oxide layer and matrix of sample PIP-5 after oxidation at 1500 °C for 5 h: (a) HAADF image and (b–g) elemental distribution maps.

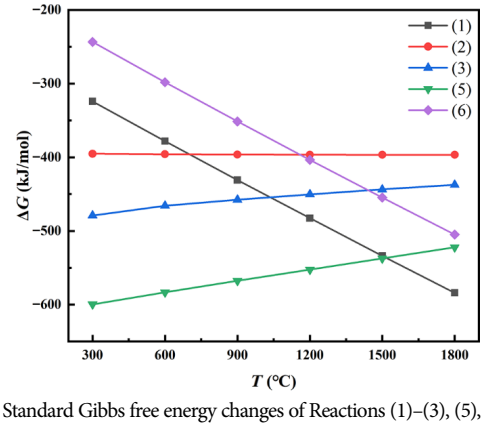

Fig. 12 Standard Gibbs free energy changes of Reactions (1)–(3), (5), and (6) as a function of temperature.

are preferentially oxidized, and oxygen diffuses through the pores formed by the oxidation of the carbon fibers and PyC in the composites.

4) The interfacial region between the oxide layer and the matrix of the 5th PIP-processed composites after oxidation at 1500 °C for 5 h mainly consisted of an amorphous dense glassy phase and an incompletely oxidized but partially crystallized matrix, and this dense glassy structure hindered the diffusion of oxygen into the interior of the composite.

Acknowledgements

This work was financially supported by the National Natural Science Foundation of China (Nos. 52372059, 52172068, 52232004, and 52002092), the Heilongjiang Natural Science Fund for Young Scholars (No. YQ2021E017), the Fundamental Research

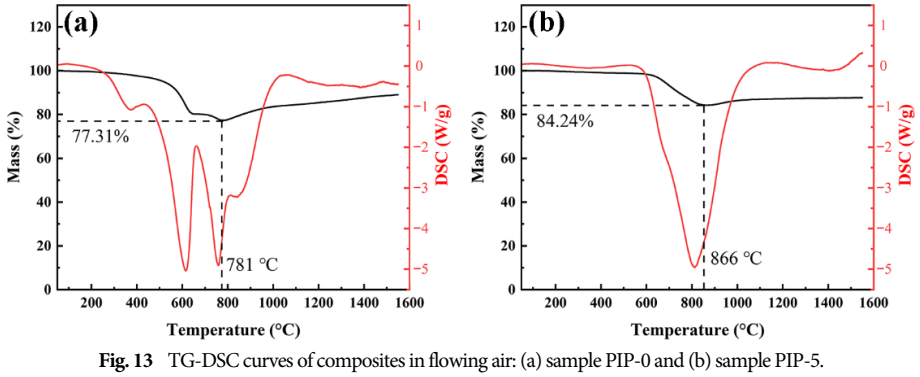

Fig. 13 TG-DSC curves of composites in flowing air: (a) sample PIP-0 and (b) sample PIP-5.

Funds for the Central Universities (No. 2022FRFK060012), the Heilongjiang Touyan Team Program, and the Advanced Talents Scientific Research Foundation of Shenzhen: Yu Zhou. This work was also funded by the Beijing Engineering Research Center of Efficient and Green Aerospace Propulsion Technology and Advanced Space Propulsion Laboratory of BICE (No. LabASP-2023-11), the Huiyan Action (No. 1A423653), and the Key Technologies R&D Program of CNBM (No. 2023SJYL05). Ralf Riedel also gratefully acknowledges the financial support provided by the Research Training Group 2561 "MatCom-ComMat: Materials Compounds from Composite Materials for Applications in Extreme Conditions" funded by the Deutsche Forschungsgemeinschaft (DFG), Bonn, Germany.

Declaration of competing interest

The authors have no competing interests to declare that are relevant to the content of this article. The author Dechang Jia is the Editorial Committee member of this journal.

Electronic Supplementary Material

Supplementary material is available in the online version of this article at https://doi.org/10.26599/JAC.2024.9220887.

References

[1] Padture NP. Advanced structural ceramics in aerospace propulsion. *Nat Mater* 2016, **15**: 804–809.

[2] Song CK, Ye F, Cheng LF, *et al.* Long-term ceramic matrix composite for aeroengine. *J Adv Ceram* 2022, **11**: 1343–1374.

[3] Ni DW, Cheng Y, Zhang JP, *et al.* Advances in ultra-high temperature ceramics, composites, and coatings. *J Adv Ceram* 2022, **11**: 1–56.

[4] Jiao XY, He QC, Tan Q, *et al.* Ablation behavior of mullite modified C/C–SiC–HfC composites under oxyacetylene torch for single and cyclic ablations with two heat fluxes. *J Eur Ceram Soc* 2023, **43**: 5851–5862.

[5] Tan Q, Jiao XY, He QC, *et al.* Effect of mullite content on microstructure and ablation behavior of mullite modified C/C–SiC–HfC composites. *Corros Sci* 2023, **222**: 111405.

[6] Jia DC, Liang B, Yang ZH, *et al.* Metastable Si–B–C–N ceramics and their matrix composites developed by inorganic route based on mechanical alloying: Fabrication, microstructures, properties and their relevant basic scientific issues. *Prog Mater Sci* 2018, **98**: 1–67.

[7] Zhang PF. Hot pressing behavior and high-temperature properties of mechanically alloyed 2Si–B–3C–N ceramic. Ph.D. Thesis. Harbin (China): Harbin Institute of Technology, 2013. (in Chinese)

[8] Liang B, Yang ZH, Li YT, *et al.* Ablation behavior and mechanism of SiC_f/C_f/SiBCN ceramic composites with improved thermal shock resistance under oxyacetylene combustion flow. *Ceram Int* 2015, **41**: 8868–8877.

[9] Liang B, Yang ZH, Jia DC, *et al.* Amorphous silicoboron carbonitride monoliths resistant to flowing air up to 1800 °C. *Corros Sci* 2016, **109**: 162–173.

[10] Wang BZ, Li DX, Yang ZH, *et al.* Study on oxidation resistance and oxidative damage mechanism of SiBCN–Ta_4HfC_5 composite ceramics. *Corros Sci* 2022, **197**: 110049.

[11] Wang BZ, Li DX, Yang ZH, *et al.* Microstructural evolution and mechanical properties of *in situ* nano Ta_4HfC_5 reinforced SiBCN composite ceramics. *J Adv Ceram* 2020, **9**: 739–748.

[12] Zhang PF, Jia DC, Yang ZH, *et al.* Microstructural features and properties of the nano-crystalline SiC/BN(C) composite ceramic prepared from the mechanically alloyed SiBCN powder. *J Alloys Compd,* 2012, **537**: 346–356.

[13] Li DX, Yang ZH, Mao ZB, *et al.* Microstructures, mechanical properties and oxidation resistance of SiBCN ceramics with the addition of MgO, ZrO_2 and SiO_2 (MZS) as sintering additives. *RSC Adv* 2015, **5**: 52194–52205.

[14] Zhang PF, Jia DC, Yang ZH, *et al.* Research on the interfacial structure and property improvement of the Cfiber/2Si–B–3C–N ceramic matrix composite. *Mater Charact* 2018, **142**: 59–67.

[15] Niu ZB, Wang BZ, Pan LJ, *et al.* Mechanical and thermal shock properties of C_f/SiBCN composite: Effect of sintering densification and fiber coating. *J Am Ceram Soc* 2022, **105**: 4321–4335.

[16] Dou WH, Li DX, Wang BZ, *et al.* Tailoring layered C_{sf}/SiBCN composites with pseudoplastic fracture behavior: Strengthening and toughening mechanisms. *J Am Ceram Soc* 2024, **107**: 404–416.

[17] Colombo P, Mera G, Riedel R, *et al.* Polymer-derived ceramics: 40 years of research and innovation in advanced ceramics. *J Am Ceram Soc* 2010, **93**: 1805–1837.

[18] Viard A, Fonblanc D, Lopez-Ferber D, *et al.* Polymer derived Si–B–C–N ceramics: 30 years of research. *Adv Eng Mater* 2018, **20**: 1800360.

[19] Weinmann M, Schuhmacher J, Kummer H, *et al.* Synthesis and thermal behavior of novel Si–B–C–N ceramic precursors. *Chem Mater* 2000, **12**: 623–632.

[20] Janakiraman N, Zern A, Weinmann M, *et al.* Phase evolution and crystallization in Si–B–C–N ceramics derived from a polyborosilazane precursor: Microstructural characterization. *J Eur Ceram Soc* 2005, **25**: 509–520.

[21] Ravi Kumar NV, Prinz S, Cai Y, *et al.* Crystallization and creep behavior of Si–B–C–N ceramics. *Acta Mater* 2005, **53**: 4567–4578.

[22] Butchereit E, Nickel KG, Müller A. Precursor-derived Si–B–C–N ceramics: Oxidation kinetics. *J Am Ceram Soc* 2001, **84**: 2184–2188.

[23] Cinibulk MK, Parthasarathy TA. Characterization of oxidized polymer-derived SiBCN fibers. *J Am Ceram Soc* 2001, **84**: 2197–2202.

[24] Chen BW, Ding Q, Ni DW, *et al.* Microstructure and mechanical properties of 3D C_f/SiBCN composites fabricated by polymer infiltration and pyrolysis. *J Adv Ceram* 2021, **10**: 28–38.

[25] Ding Q, Ni DW, Wang Z, *et al.* 3D C_f/SiBCN composites prepared by an improved polymer infiltration and pyrolysis. *J Adv Ceram* 2018, **7**: 266–275.

[26] Ma BS, Wang YG. Fabrication of dense polymer-derived silicon carbonitride ceramic bulks by precursor infiltration and pyrolysis processes without losing piezoresistivity. *J Am Ceram Soc* 2018, **101**: 2752–2759.

[27] Yu YX, Dou WH, Xu J, *et al.* Fabrication of high gas-tightness SiCN ceramic via PIP process for increasing sensing distance of pressure sensor. *Ceram Int* 2020, **46**: 2155–2162.

[28] Feng B, Zhang Y, Li BY, *et al.* Medium-temperature sintering efficiency of ZrB_2 ceramics using polymer-derived SiBCN as a sintering aid. *J Am Ceram Soc* 2019, **102**: 855–866.

[29] Zhu SM, Fahrenholtz WG, Hilmas GE. Enhanced densification and mechanical properties of ZrB_2–SiC processed by a preceramic polymer coating route. *Scripta Mater* 2008, **59**: 123–126.

[30] Kim S, Chae JM, Lee SM, *et al.* Change in microstructures and physical properties of ZrB_2–SiC ceramics hot-pressed with a variety of SiC sources. *Ceram Int* 2014, **40**: 3477–3483.

[31] Bernardo E, Ponsot I, Colombo P, *et al.* Polymer-derived SiC ceramics from polycarbosilane/boron mixtures densified by SPS. *Ceram Int* 2014, **40**: 14493–14500.

[32] Jia Y, Chen SA, Ji XY, *et al.* High-temperature oxidation behavior and oxidation mechanism of C/SiBCN composites in static air. *Ceram Int* 2019, **45**: 12764–12772.

[33] Luan XG, Xu XM, Wang L, *et al.* Long-term oxidation behavior of C/SiC–SiBCN composites in wet oxygen environment. *J Eur Ceram Soc* 2021, **41**: 1132–1141.

[34] Wang BZ. Microstructure evolution and high temperature oxidation and ablation mechanism of mechanical alloying nano-Ta_4HfC_{5p}/

SiBCN powder and ceramics. Ph.D. Thesis. Harbin (China): Harbin Institute of Technology, 2022. (in Chinese)
[35] Colombo P. *Polymer Derived Ceramics: From Nano-structure to Applications*. Pennsylvania (USA): DEStech Publications, Inc., 2010.
[36] Palmer DC, Hemley RJ, Prewitt CT. Raman spectroscopic study of high-pressure phase transitions in cristobalite. *Phys Chem Miner* 1994, **21**: 481–488.
[37] Lamouroux F, Bourrat X, Nasalain R, *et al*. Structure/oxidation behavior relationship in the carbonaceous constituents of 2D-C/PyC/SiC composites. *Carbon* 1993, **31**: 1273–1288.